Gadolinium Chloride Augments Tumor-Specific Imaging of Targeted Quantum Dots *In Vivo*

Parmeswaran Diagaradjane,[†] Amit Deorukhkar,[†] Juri G. Gelovani,[‡] Dipen M. Maru,[§] and Sunil Krishnan[†,*]

[†]Departments of Radiation Oncology, [‡]Experimental Diagnostic Imaging, and [§]Pathology, The University of Texas M. D. Anderson Cancer Center, Houston, Texas 77030

The clinical success of targeted therapeutic agents for cancer treatment has fueled an interest in techniques to noninvasively image tumors before, during, and after targeted therapy to assess treatment efficacy.[1] One such opportunity for repetitive real-time noninvasive quantitative imaging is optical imaging using nanoparticle biosensors.[2] Semiconductor quantum dots (QDs), which have unique size- and composition-dependent tunable emission from visible to near-infrared wavelengths, high fluorescence quantum yield, and photostability, facilitate quantitative optical imaging.[3−8] Numerous studies have reported the use of unconjugated and conjugated QDs for *in vivo* imaging of tumor vasculature,[9−14] sentinel lymph nodes,[15−21] tumor-specific receptors,[22−28] and tumor immune responses.[29] Despite the promising results achieved with these QD imaging probes, however, issues remain that hinder the translation of these probes from the bench to the bedside, including (i) degradation of the image quality of tumor-specific signals due to significant background noise arising from QDs sequestered in the liver and spleen, which is a result of the rapid clearance of QDs from the circulation by the reticulo-endothelial system (RES),[30] and (ii) concerns about the biocompatibility of QDs, particularly the long-term effects of compounds that are composed of heavy metals and retained for long durations within the body.[31,32]

A potential solution to the entrapment of QDs in the liver, a determinant of both long-term retention (and toxicity) and nonspecific background signal in imaging applications, is to minimize the detection and capture of nanoparticles by the RES. Reducing nonspecific sequestration by RES mac-rophages could potentially improve the circulatory half-life of nanoparticles, resulting in target-specific accumulation within tumors, which would be particularly helpful for imaging applications. Earlier attempts to alter the biodistribution of nanoparticles to enhance target-specific accumulation have focused on (i) surface modification of nanoparticles to evade RES capture[6,8,30,33−35] or (ii) inhibiting RES uptake by saturating RES capacity or blocking RES activity.[36−40] Unfortunately, neither strategy has yielded a reliable and reproducible class solution to the problem of dampened signal-to-noise ratios in nanoparticle-based imaging.

Here, we propose using gadolinium chloride (GdCl₃), a Kupffer cell deactivator,[41] to suppress RES macrophage activity and thereby increase the fraction of QDs within the circulation. The consequent increase in the circulatory half-life of QDs modified the kinetics of tumor-specific accumulation of conjugated QDs, resulting in a greater than 50% increase in tumor-specific uptake after systemic administration of QDs. Compartment model analysis revealed rate parameters that corroborated the observed shift in kinetics. *In vivo* contrast enhancement was validated by findings on *ex vivo* imaging, measurement of

ABSTRACT Nonspecific sequestration of nanoparticles by the reticulo-endothelial system (RES) results in the degradation of image quality of nanoparticle-based imaging. We demonstrate that gadolinium chloride (GdCl₃) pretreatment inactivates RES macrophages, thereby increasing circulatory time and amplifying the tumor-specific signal of conjugated nanoparticles *in vivo*. The experimental results were validated using compartmental modeling, and the rate parameters for the observed kinetics pattern were estimated. This pretreatment strategy could have broad applicability across biomedical applications utilizing theranostic nanoparticles that are sequestered by the RES.

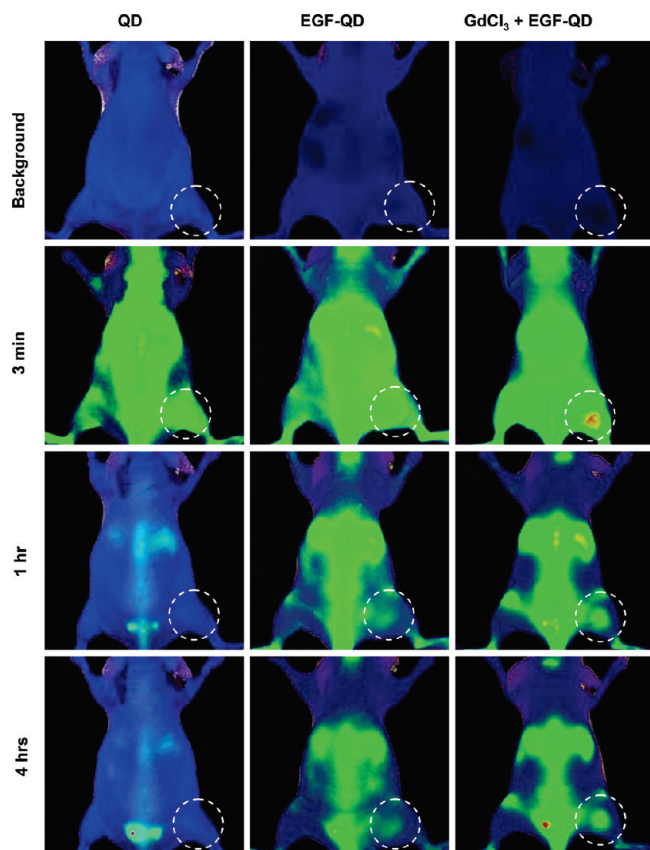*Address correspondence to skrishnan@mdanderson.org.

Figure 1. *In vivo* fluorescence images of animals at 0 h (Background), 3 min, 1 h, and 4 h after intravenous injection of QD, EGF-QD, or GdCl₃ pretreatment followed by EGF-QD.

fluorescence of tissue extracts, confocal fluorescence microscopy, immunostaining, and transmission electron microscopy of Kupffer cell populations in the liver.

RESULTS AND DISCUSSION

GdCl₃ Improves Tumor-to-Background Ratio of Tumors Imaged with Receptor-Targeted QDs. Recently, we reported the synthesis and characterization of an epidermal growth factor (EGF)-conjugated QD nanoprobe (EGF-QD) to image EGF receptor (EGFR) in human tumor xenografts in mice.[22] An amine-functionalized CdSeTe/ZnS (core/shell) QD with an emission maximum at 800 nm was coupled to reduced EGF with free sulfhydryl groups through a heterobifunctional cross-linker, 4-(maleimidomethyl)-1-cyclohexanecarboxylic acid *N*-hydroxysuccinimide ester, to form an EGF-QD nanoprobe. Quantitative *in vivo* optical imaging of EGFR overexpression in subcutaneous xenograft tumors was feasible 4 h after intravenous injection of the EGF-QD nanoprobe. However, the intensity of tumor-specific fluorescence was partially eclipsed by liver fluorescence due to nonspecific uptake of QDs by the RES.

For this study, we utilized similar imaging techniques and probes to perform serial imaging of animals bearing subcutaneous EGFR-overexpressing tumor xenografts after intravenous injection of a 10 pmol QD equivalent/mouse of (a) unconjugated QD, (b) EGF-

QD, or (c) GdCl₃ (10 mg/kg) 24 h prior to EGF-QD. The concentration of GdCl₃ (10 mg/kg corresponding to ~40 μmol/kg) chosen for this study is based on earlier reports where GdCl₃ is used for the blockade of Kupffer cell activity[42−48] and is below the toxic threshold limit of ~300 μmol/kg.[49] To separate the autofluorescence from the QD signal, the images were spectrally unmixed using NIH Image J software. The spectrally unmixed QD fluorescence images and the autofluorescence images were remixed to form a composite image. The background images of representative animals from the three groups prior to the injection of probe and their corresponding images at 3 min, 1 h, and 4 h postinjection are shown in Figure 1. Immediately after injection of probe (~3 min), all three groups demonstrated enhanced fluorescence intensity in the tumor region. This is largely a reflection of the increased vascular volume and permeability of the tumor xenograft. One hour after injection of QD, the fluorescence intensity within the tumor had decreased significantly and returned to near-baseline levels. Although a similar decrease in the fluorescence signal was observed 1 h after injection of EGF-QD, the fluorescence intensity did not reach baseline levels, probably as a result of some receptor-specific binding within the EGFR-overexpressing tumor. Four hours after injection, both the EGF-QD group and the GdCl₃ pretreatment plus EGF-QD group demonstrated an increase in the fluorescence signal within the tumor; however, the GdCl₃ pretreatment plus EGF-QD group exhibited a higher intensity within the tumor than the EGF-QD alone group. The higher fluorescence intensity observed within the tumor in both groups compared to the QD group could be attributed to the conjugated probe specifically binding to the tumor EGFR. We hypothesized that the higher fluorescence intensity observed in the GdCl₃ pretreatment plus EGF-QD group than in the EGF-QD alone group is attributable to the increased circulatory half-life of the probe resulting from inhibition of Kupffer cell activity.

GdCl₃ Pretreatment Alters the Pharmacokinetics of Receptor-Targeted QDs. A detailed analysis of the kinetic pattern of tumor enhancement was performed using tumor-to-background ratios (TBRs) calculated from the intensity values within the regions of interest in the tumor and in the shoulder (background) of the mouse. As reported above, tumor signals in animals injected with EGF-QD demonstrated an initial rapid influx (~3 min postinjection) followed by a rapid clearance phase, reaching an apparent dynamic equilibrium condition approximately 1 h after injection. Beyond the apparent dynamic equilibrium state, an accumulation phase was observed, during which the fluorescence intensity in the tumor peaked around 4 to 6 h postinjection followed by a gradual decrease toward near-baseline levels at 24 h (see the Supporting Information, Figure S1). Animals injected with QD alone exhibited similar initial rapid influx followed by a clearance phase. However, no accu-
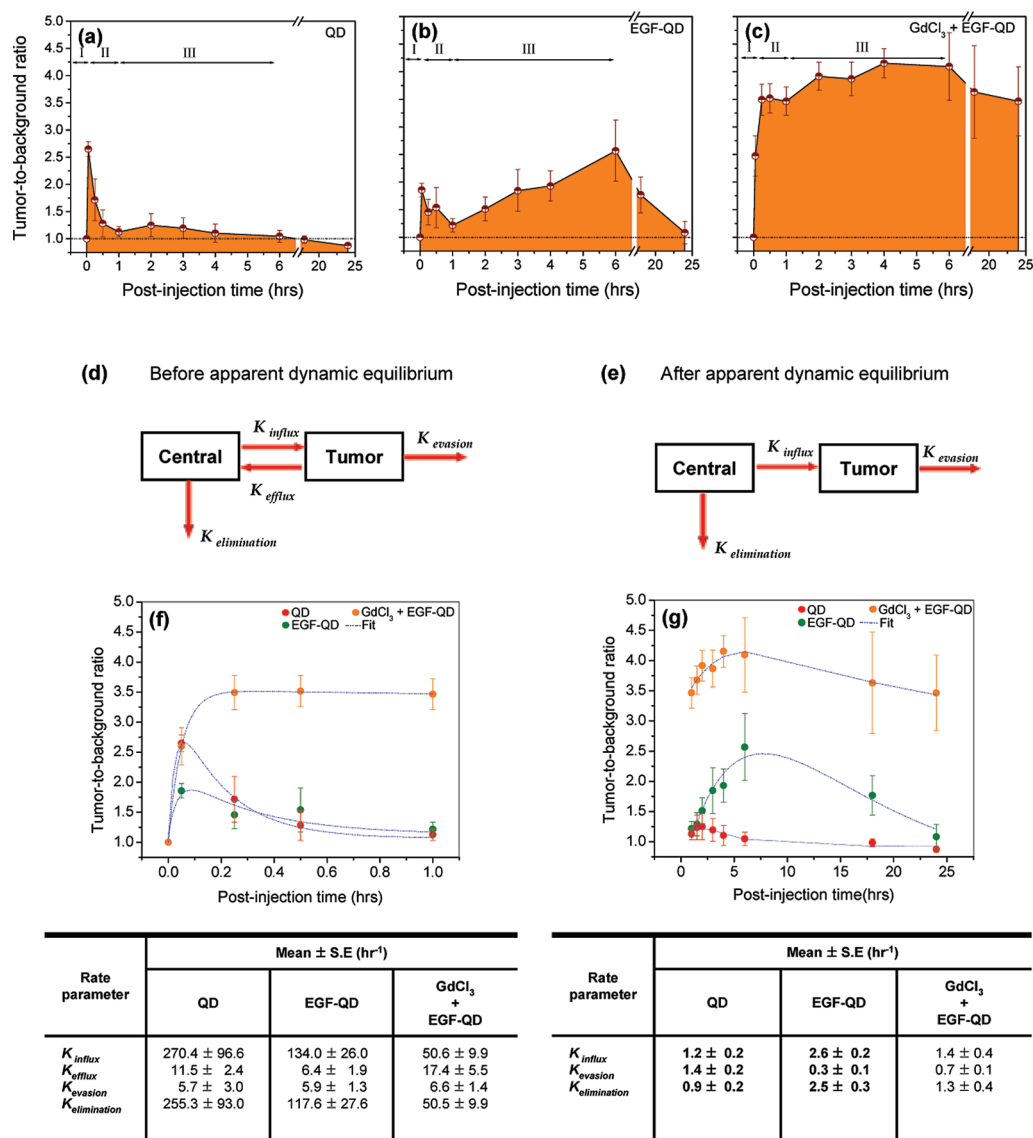
Figure 2. Estimated mean tumor-to-background ratios (mean ± SE) from animals injected with (a) QD, (b) EGF-QD, or (c) GdCl$_3$ followed by EGF-QD. The three phases of influx, efflux, and accumulation are represented as I, II, and III, respectively. On the basis of the observed kinetic pattern, a two-compartment model was proposed to estimate the kinetic rate parameters (d) before and (e) after apparent dynamic equilibrium. The two-compartment model fit (blue dotted lines) to the tumor-to-background ratios before and after dynamic equilibrium is illustrated in (f) and (g), respectively, with the corresponding rate parameters represented in tables below the figure.

mulation phase was observed. In contrast to these observations, while GdCl$_3$ pretreatment resulted in a rapid influx phase similar to that seen after QD alone and after EGF-QD, the subsequent clearance phase was considerably dampened (Figure 2a−c). The lack of a pronounced clearance phase could be attributed to the prolonged circulatory half-life of the probe due to blockade of liver sequestration, resulting in early initiation of receptor-specific binding within the tumor. One hour postinjection an apparent dynamic equilibrium was attained, with a significantly higher mean TBR ± standard error with GdCl$_3$ pretreatment (3.4 ± 0.25) than without GdCl$_3$ pretreatment (1.2 ± 0.11). Beyond this state of apparent dynamic equilibrium, increasing receptor-specific binding led to eventual saturation of

receptors around 4 to 6 h postinjection followed by a gradual decrease until 24 h postinjection.

Compartmental Modeling of Nanoprobe Kinetics. On the basis of the observed kinetic pattern, compartment models were proposed to estimate the rate parameters before and after the apparent dynamic equilibrium state. The schemes for the two-compartment models are illustrated in Figure 2d,e, respectively. Each model consists of two compartments, the central compartment and the tumor compartment, representing the circulatory system and the tumor, respectively, with the assumption that the imaging probe is homogenously distributed in both of these compartments. The probe content in the central compartment immediately after injection is denoted as M. At any given postinjection time,

the probe content in the central compartment is dependent on the distribution in various organs and the tumor and the uptake by RES. Hence, the amount of probe that is available in the central compartment at time, t, can be represented as $dM/dt = -kM$, where k is the rate parameter representing the distribution of the probe in the organs including tumor and is represented as

$$k = \sum_{organs} k_{elim} + k_{inf}^{tumor}$$

in which

$$\sum_{organs} k_{elim} = \sum_{organs} k_{dist} + k_{exc}$$

and k_{inf}^{tumor} is the influx into the tumor tissues. The parameter $\sum_{organs} k_{dist}$ represents the elimination of the nanoprobe through the distribution in organs and by excretion k_{exc}. The elimination resulting from excretion was not included in this model, as we did not observe any excretion of probe in the urinary or fecal discards within 24 h after the injection ($k_{exc} \cong 0$), which is in accordance with earlier reports.[22]

At $t = 0$, $M = M_0$, and thus the amount of probe in the central compartment at a given time t can be represented as $M = M_0 e^{-kt}$, where M is the amount of probe in the central compartment at time t. Similarly, the probe content in the tumor compartment is denoted as Q_t at a given postinjection time. Immediately after injection, the amount of probe in the tumor tissues increases rapidly due to high influx. However, due to the high interstitial tumor pressure, fast clearance or efflux is observed until the apparent dynamic equilibrium state is reached. Once the equilibrium state is attained, the efflux, or back flow, from the tumor is considered to be negligible. On the basis of this assumption, two separate compartment models are proposed for the kinetics patterns observed before and after the apparent dynamic equilibrium state.

Before the apparent dynamic equilibrium is reached, the probe content in the tumor compartment at a given time point is dependent on the probe distribution to various organs, influx into tumor, and evasion from tumor. The amount of probe in the tumor, Q_t, at a given time point t ($0 < t < 1$) can be represented as

$$\frac{dQ_t}{dt} = k_{inf}M - (k_{eff} + k_{ev})Q_t \quad (1)$$

where, k_{inf}, k_{eff}, and k_{ev} represents the rate parameters for probe influx due to initial perfusion, efflux due to high interstitial tumor pressure, and evasion through the lymphatics.

After apparent dynamic equilibrium is reached, the efflux from the tumor is negligible, and the probe accumulation in the tumor was assumed to be predominant. Hence, the amount of probe in the tumor, Q_t, at a given time point t ($1 < t < 24$) can be represented as

$$\frac{dQ_t}{dt} = k_{inf}M - k_{ev}Q_t \quad (2)$$

Substituting the value of M and solving eqs 1 and 2 gives Q_t, the amount of probe present in the tumor tissue.

$$Q_t \atop 0 \leq t \leq 1 \text{ h} = \frac{M_0 k_{inf}}{(k_{eff}+k_{ev}) - (k_{inf} + k_{elim})}\{e^{-(k_{inf}+k_{elim})t} - e^{-(k_{eff}+k_{ev})t}\} + C \quad (3)$$

$$Q_t \atop 1 \leq t \leq 24 \text{ h} = \frac{M_0 k_{inf}}{(k_{eff}-k_{ev})}\{e^{-k_{ev}t} - e^{-k_{eff}t}\} + C \quad (4)$$

where M_0 and C in eqs 3 and 4 represent the baseline value at the lower limit of the postinjection time and proportionality constants, respectively. The estimated TBR values obtained from *in vivo* imaging of individual animals were fit to the above equations with a nonlinear fitting module using Microcal Origin (OriginLab, Northampton, MA). The curve fitting was performed using the Levenberg−Marquardt algorithm, and the goodness of fit was estimated using nonlinear least-squares regression with a confidence band of 0.95. For all of the curve fits, the R^2 values were observed to be $1.0 > R^2 > 0.85$. The rate parameters before and after apparent dynamic equilibrium are summarized below Figure 2f,g, respectively.

Prior to the apparent dynamic equilibrium, the kinetics of QDs and EGF-QDs follow similar patterns (Figure 2f). The rapid influx and efflux observed in the first few minutes postinjection are reflective of the increased permeability of tumor vasculature, a component of the enhanced permeability and retention (EPR) effect of tumors.[50] However, a comparison of rate parameters averaged across the first hour demonstrates that there was a faster influx (~2-fold) of QDs than EGF-QDs. Similarly, the rate of efflux of probe into the central compartment was higher (~1.8-fold) for QDs than for EGF-QDs. The higher influx and efflux rates observed with QDs are attributable to the smaller size of QDs (~20 nm *vs* ~26 nm for EGF-QDs). As noted in the table below Figure 2f, the evasion rates are relatively low across all groups and are less prominent contributors to the observed kinetics of particles. Due to differences in kinetic patterns between the groups with and without GdCl$_3$ pretreatment, a direct comparison of rate parameters averaged across the first hour is difficult. However, one parameter that is less influenced by vascular permeability (*i.e.*, the EPR effect noted in the first few minutes postinjection) of the tumor is the probe elimination rate from the central compartment. Furthermore, since trafficking of particles into and from tumors is only a small component of probe concentrations within the central compartment, this rate of elimination (averaged over

the first hour), a variable that can be compared across groups, is a key determinant of circulatory volume of the probe. A comparison of the rate of elimination of the probe from the central compartment demonstrates that EGF-QD injection following $GdCl_3$ pretreatment is lesser than (nearly half) that of EGF-QD injection without $GdCl_3$ pretreatment. This suggests that Kupffer cell inactivation by $GdCl_3$ pretreatment results in a smaller fraction of the probe extracted from the central compartment during every circulatory pass through the liver and, hence, a greater circulatory time and concentration that permits gradual accumulation/binding of the probe to the tumor. This contributes to the TBR of ~3.5 that is achieved with $GdCl_3$ pretreatment within the first hour postinjection of EGF-QD and maintained thereafter (Figure 2g). These modeling results corroborate our initial expectation that particle size influences initial influx and efflux rates and that peripheral extraction efficiency (primarily by Kupffer cells in the liver) influences circulatory concentrations and thereby tumor accumulation kinetics.

$GdCl_3$ Influences QD Accumulation in the Liver at the Organ, Tissue, And Cellular Levels. *Ex vivo* fluorescence images of organs from all of the groups of animals 4 h postinjection are shown in Figure 3a—d. The liver and spleen demonstrated higher fluorescence intensity following EGF-QD injection with or without $GdCl_3$ pretreatment than with QD injection alone. This is a reflection of the previously seen receptor-specific binding of the EGF-conjugated probe to abundant mouse EGFR in the mouse liver. Apart from the liver and spleen, the lymph nodes were prominent sites of increased fluorescence intensity. All other organs demonstrated relatively low fluorescence intensity. However, following EGF-QD injection, the tumor tissues demonstrated higher fluorescence intensity when pretreated with $GdCl_3$ than when $GdCl_3$ was not administered. These results clearly indicate that suppression of Kupffer cell activity significantly increased the fraction of injected probe that reaches and binds to its target within tumors, thereby enhancing visualization of the tumor. The *ex vivo* fluorescence results were further validated by measuring the fluorescence intensity of tissue extracts from the tumor and liver (Figure 3e). The mean radiance per milligram of tissues was calculated based on the weight of the extracted tissue. Pretreatment with $GdCl_3$ before EGF-QD injection significantly ($p < 0.001$) increased the fluorescence intensity of tumors.

Confocal microscopy of frozen tissue sections from the liver, tumor, and lymph nodes further validated the observed results (Figure 4). A significant decrease in fluorescence was observed in the liver tissue sections following pretreatment with $GdCl_3$ when compared to the liver tissues from animals that were not pretreated with $GdCl_3$. A similar trend was observed with fluorescence confocal images of the lymph nodes, suggesting macrophage inactivation in the lymph
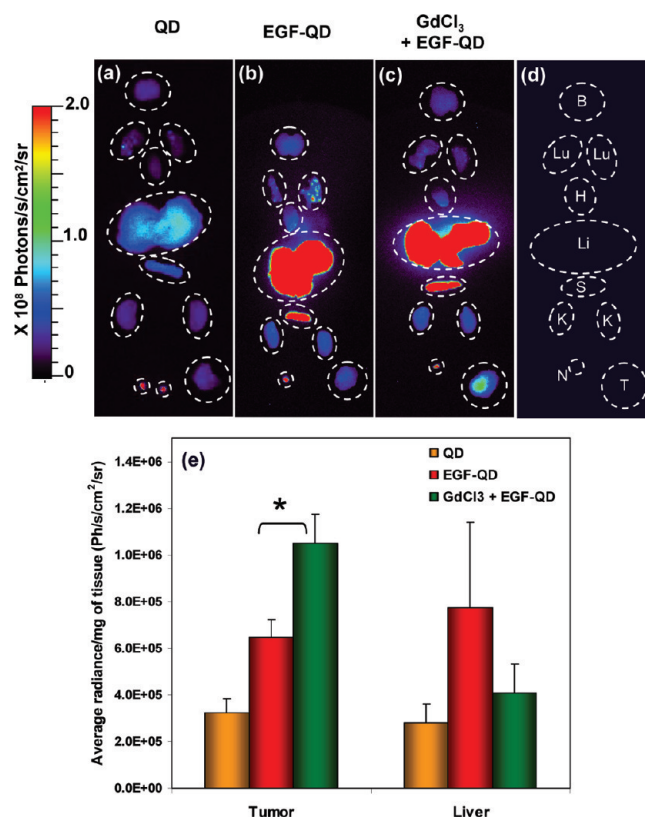

Figure 3. *Ex vivo* fluorescence images of organs harvested 4 h after (a) QD injection, (b) EGF-QD injection, and (c) $GdCl_3$ pretreatment followed by EGF-QD injection. (d) Cartoon representing the arrangement of organs where B, Lu, H, Li, S, K, N, and T represent the brain, lungs, heart, liver, spleen, kidney, lymph node, and tumor, respectively. The corresponding fluorescence levels (mean ± SE) from the extracts of tumor and liver tissues are represented in (e), where ∗ represents the statistical significance ($p < 0.001$) based on an unpaired Student's *t* test.

nodes, as well. In contrast, more pronounced tumor fluorescence that was uniformly distributed through-
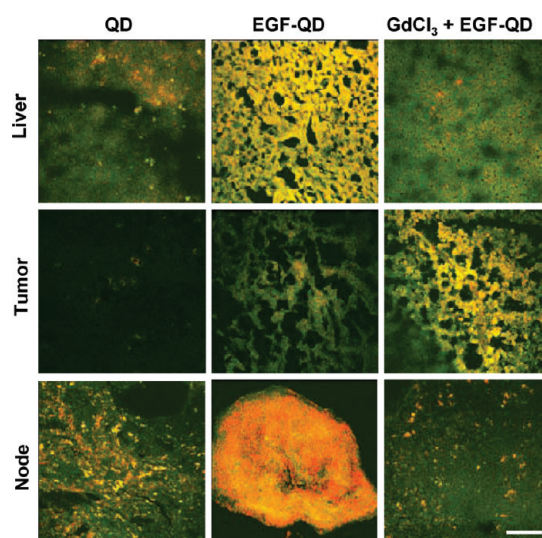

Figure 4. Fluorescence confocal images of frozen liver, tumor, and lymph node extracted 4 h after QD injection, EGF-QD injection, and $GdCl_3$ pretreatment followed by EGF-QD injection. Green represents autofluorescence, and red represents QD fluorescence (scale bar = 50 μm).
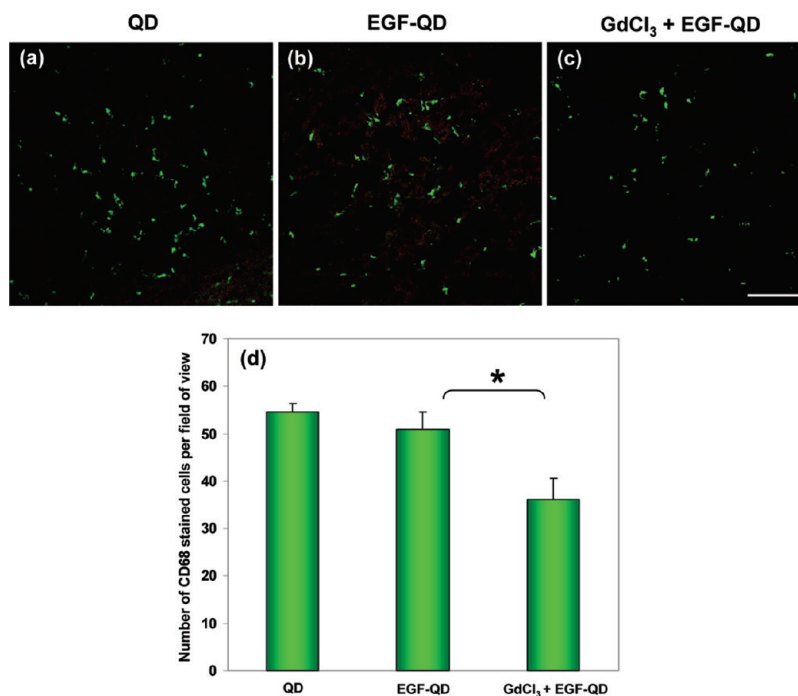
Figure 5. Activated Kupffer cell-specific anti-CD68 immunofluorescence staining of liver tissues extracted 4 h after (a) QD injection, (b) EGF-QD injection, and (c) GdCl$_3$ pretreatment followed by EGF-QD injection. Green represents CD68 staining, and red represents QD fluorescence (scale bar = 50 μm). (d) Quantified CD68-stained activated Kupffer cells in the liver tissues from each group averaged over different field of views ($n = 7$) show statistically significant ($p < 0.001$) difference with and without GdCl$_3$ pretreatment.

out the tumor parenchyma was observed with EGF-QD injection following GdCl$_3$ pretreatment than with EGF-QD injection alone. As previously described, a patchy pattern of minimal fluorescence was observed after QD injection alone.

The effect of GdCl$_3$ on Kupffer cell activity in liver tissues was assessed by immunofluorescence staining using a primary anti-CD68 antibody, a marker for activated macrophages, and a secondary fluorescein isothiocyanate (FITC)-conjugated Affinipure secondary antibody. While there was some overlap between stained activated Kupffer cells and QD fluorescence in the liver of mice injected with EGF-QD, there were areas of QD accumulation in the absence of activated Kupffer cells, suggesting that clumps of QDs may be trapped within hepatic sinusoids or within hepatocytes themselves. Nevertheless, there were fewer activated Kupffer cells in the livers of mice pretreated with GdCl$_3$ than in those without GdCl$_3$ pretreatment (Figure 5). Further, fewer areas of QD fluorescence seen in the livers of mice pretreated with GdCl$_3$ are potentially attributable to the effect of GdCl$_3$ on the intrahepatic distribution of QDs, corroborating earlier reports on the alteration of intrahepatic distribution of smaller particles by GdCl$_3$.[47] Quantification of anti-CD68 positive cells revealed statistically significantly ($p < 0.001$) fewer activated Kupffer cells in the livers of mice pretreated with GdCl$_3$ than those of mice without GdCl$_3$ pretreatment (Figure 5d).

To visualize the geographical distribution of these activated Kupffer cells within the hepatic parenchymal architecture, liver sections were also analyzed by immunohistologic staining with the same primary antibody. Fewer activated Kupffer cells were observed in the GdCl$_3$ pretreatment group than in the EGF-QD alone group (see the Supporting Information, Figure S2). Lastly, the ultrastructural architecture and cellular composition of the livers in these mice were imaged and analyzed using transmission electron microscopy. While the number of Kupffer cells was not significantly different between the GdCl$_3$-pretreated and non-GdCl$_3$-pretreated mice, there were more Kupffer cells lining the sinusoidal spaces and more Kupffer cells within endocytotic vesicles harboring clumps of QDs in the non-GdCl$_3$-pretreated livers (Figure 6).

We demonstrate that GdCl$_3$ pretreatment enhances the signal-to-noise ratio in optical imaging applications using conjugated nanoparticles. Inactivation of RES macrophage activity with GdCl$_3$ results in alteration of the pharmacokinetics of the probe that can be compartmentally modeled. We anticipate that this simple technique will have broad clinical applicability in biomedical imaging applications utilizing most classes of metallic nanoparticles that are sequestered in the liver.

A variety of techniques have been employed to reduce nonspecific uptake of QDs by the liver to enhance the signal-to-noise ratio of conjugated nanoparticle-based imaging.[6,8,30] The most commonly used strategy is to modify the surface chemistry of the
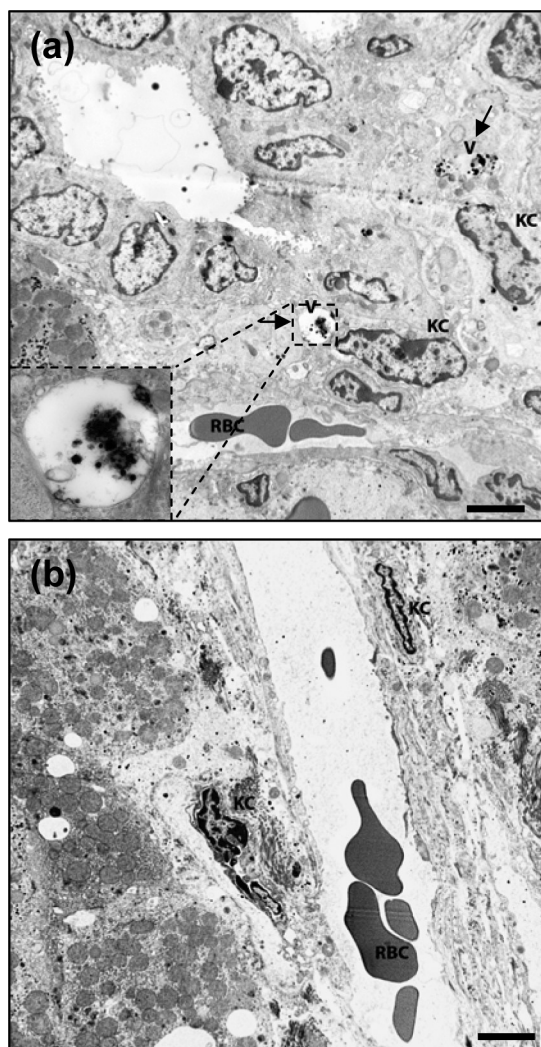
Figure 6. Transmission electron microscopy image of liver tissue extracted 4 h after (a) EGF-QD injection and (b) GdCl₃ pretreatment followed by EGF-QD injection. The arrows in (a) represent the accumulation of QDs in the endocytotic vesicles within the Kupffer cells, and the inset represents the enlarged version of the vesicles containing the QDs. The labels V, KC, and RBC represent the vesicles, Kupffer cells, and red blood cells, respectively (scale bar = 5 μm).

nanoparticle to evade detection and engulfment by the numerous macrophages within the RES. For instance, the surface of the nanoparticle may be coated with biocompatible hydrophilic surfactants, such as polyethylene glycol (PEG) or block copolymer, which reduce opsonization and detection by the RES.[30,51−54] However, high molecular weight PEGylation increases the effective hydrodynamic diameter of nanoparticles, resulting in altered biodistribution in the target. Nevertheless, most QDs are PEGylated to improve circulation time. This does not, however, obviate the need for further reduction in liver uptake. The composition of terminal groups on the PEG coating allows conjugation and decoration of particles with biomolecules (*e.g.*, proteins and nucleic acids) that assist with homing the nanoparticle to a target organ.[55] However, these terminal groups also dictate the fate of the nanoparticle within the liver in that albumin or carboxyl groups increase clearance by the RES compared to amine groups.[56] Alternatively, saturating the RES capacity for nanoparticle clearance by pretreating the RES with large doses of unconjugated nanoparticles or latex beads has resulted in transient increases in circulatory levels of multilamellar/unilamellar vesicles and reverse-phase evaporation vesicles.[57] However, these approaches involve significantly loading the liver and the RES with large doses of molecules that are retained indefinitely within the body.

Other pretreatment strategies using the same principles include the use of dextran sulfate or methyl palmitate, which are toxic to hepatic macrophages.[36,57] Though these approaches are capable of minimally reducing RES uptake, they do not significantly reduce biodistribution in the target tissues. Another potentially useful strategy to eliminate the uptake by the RES is to reduce the size of the nanoparticle to 5−6 nm (*i.e.*, below the renal filtration threshold) for rapid and efficient renal clearance of the probe.[58] However, since larger QD sizes are needed to obtain fluorescence emissions at higher (*i.e.*, red and near-infrared) wavelengths, which in turn overcomes tissue autofluorescence and improves imaging depth, decreasing the size of the QDs could potentially limit their imaging capabilities.[59] Furthermore, QDs with diameters of approximately 9 nm (*i.e.*, greater than the renal filtration threshold) directly extravasate out of normal blood vessels into interstitial fluid, resulting in a nonspecific distribution of the imaging probe.[58]

Although the aforementioned strategies have enhanced the circulatory half-life of imaging probes, there are no reports of significant contrast enhancement in target tissues. Furthermore, these strategies are time-consuming, difficult to standardize, and not applicable across most classes of nanoparticles; also, these strategies might alter the binding affinity and specificity of conjugated nanoparticles. The strategy proposed in this study has some distinct advantages. First, our approach does not depend on altering the nanoparticle itself, eliminating the need for adopting a uniform surface modification protocol for broad applicability across all nanoparticle-based imaging probes. Instead, inhibiting RES macrophage activity is likely to serve as a *class solution* to the challenge of nonspecific nanoparticle accumulation in the liver. However, extensive investigations are needed to address the challenges related to the interference of GdCl₃ with magnetic resonance imaging of paramagnetic nanoparticles since GdCl₃ does alter proton T_1 and T_2 relaxation, albeit to a different extent than gadolinium chelated to agents like DTPA. Second, this approach has been undertaken extensively in preclinical animal models of liver transplantation, where engraftment of transplanted cells is improved in the presence of GdCl₃ that inhibits Kupffer cell mediated

hepatocyte transplantation-induced liver inflammation and ischemia—reperfusion injury.[60−62] GdCl$_3$ has been generally regarded as safe in these preclinical models. Third, reducing the retention of QDs within the liver reduces the probability of deterministic late side effects, an area of concern for QD biocompatibility in clinical use.

Taken together, our results illustrate the utility of GdCl$_3$ pretreatment for enhancing the signal-to-noise ratio in optical imaging applications using nanoparticles. We demonstrated that inactivation of RES mac-rophage activity with a simple pretreatment strategy altered the kinetics and dynamics of tumor imaging with a conjugated nanoprobe. We also demonstrated that the consequent alteration in the pharmacokinetics of the nanoparticles can be compartmentally modeled. Lastly, we established the mechanism of action of GdCl$_3$ at the cellular level within hepatic tissues. This method of enhancing the signal-to-noise ratio is likely to be effective across most classes of metallic nanoparticles that are sequestered in the liver, making it broadly applicable for biomedical imaging applications.

MATERIALS AND METHODS

Materials. DMEM/Ham's F-12 50/50 mix with L-glutamine was purchased from Mediatech, Inc. (Herndon, VA). Fetal bovine serum and penicillin—streptomycin were purchased from Hyclone (Logan, UT) and Invitrogen Corporation (Carlsbad, CA), respectively. Phosphate-buffered saline (PBS) powder and gadolinium (III) chloride hexahydrate (GdCl$_3$ · 6H$_2$O) were purchased from Sigma-Aldrich (St. Louis, MO). The 800 nm QD (QD) and the antibody conjugation kit were purchased from Molecular Probes (Invitrogen). Human recombinant EGF was purchased from BD Biosciences (Bedford, MA). Rat monoclonal [FA-11] anti-CD68 antibody was purchased from Abcam Inc. (Cambridge, MA), and fluorescein isothiocyanate (FITC)-conjugated Affinipure goat anti-rat immunoglobulin G (IgG) was purchased from Jackson Immunoresearch Laboratories Inc. (West Grove, PA). Nonstick microcentrifuge tubes for preparing the QD conjugates were purchased from VWR International (West Chester, PA). Alfalfa-free diet for the animals was purchased from Dyets, Inc. (Bethlehem, PA).

Epidermal Growth Factor (EGF) Conjugation with QD. The details of the conjugation process and the characterization of the conjugated EGF-QD nanoprobe are reported elsewhere.[22] In brief, the amine-functionalized CdSeTe/ZnS (core/shell) QD (~2.0 μM, 125 μL) with fluorescence emission maximum at 800 nm was activated using 10 mM of noncleavable and membrane-permeable heterobifunctional cross-linker, 4-(maleimidomethyl)-1-cyclohexanecarboxylic acid N-hydroxysuccinimide ester (SMCC), at room temperature (rt, 21 °C) for 1 h. The activated QD was eluted with PBS (pH 7.4) through a gel-filtration PD-10 desalting column containing Sephadex G-25 (Amersham Biosciences, Piscataway, NJ). Parallely, human recombinant EGF (1 mg/mL, 300 μL) was reacted with 20 mM DTT for 30 min at rt to obtain reduced EGF with free sulfhydryl groups. The reduced EGF was purified by elution with PBS (pH 7.4) through a gel-filtration PD-10 column containing Sephadex G-25. Upon completion of these two reactions, the activated QD (the end product of step 1) and reduced EGF (the end product of step 2) were reacted for 1 h at rt to form the conjugate. The conjugation reaction was quenched by 10 mM β-mercaptoethanol, concentrated by ultracentrifugation for 15 min at 7000 rpm, and purified by eluting with PBS through a gel-filtration PD-10 column containing Superdex-200. The concentrations of QD and EGF in the final purified EGF-QD nanoprobe was estimated as 0.75 and 2.9 μM, using the known molar extinction coefficients ($\varepsilon_{550} = 17 \times 10^5$ M^{-1} cm^{-1} and $\varepsilon_{277} = 4.12 \times 10^4$ M^{-1} cm^{-1}) of QD and EGF at 550 and 277 nm, respectively.

Cell Lines and Tumor Xenografts. Colorectal cancer cell line HCT116 was obtained from the American Type Culture Collection (Manassas, VA), maintained at 37 °C in a humidified atmosphere containing 5% CO$_2$ in the appropriate growth medium supplemented with 1% penicillin—streptomycin. Six- to eight-week-old immunocompromised male nude mice (Swiss nu/nu; $n = 23$) weighing 20—25 g each were purchased from the specific pathogen-free breeding colony in the Department of Experimental Radiation Oncology, The University of Texas M. D. Anderson Cancer Center. The animals were kept in well-ventilated polypropylene cages with a 12 h light—dark cycle and fed steril-

ized standard laboratory diet and water *ad libitum*. Approval from the Institutional Animal Care and Use Committee was obtained for all experimental procedures. Near-confluent HCT116 cells grown in culture flasks were harvested using 0.05% trypsin-EDTA, centrifuged, and resuspended in sterile PBS to obtain a final cell concentration of ~2 × 10^6 cells per 50 μL, which was injected subcutaneously into the right flank of the mice. After the injection, animals were fed with a special alfalfa-free diet (to minimize the fluorescence interference from the standard laboratory diet), and tumor growth was monitored daily. Once the tumors reached 0.8—1.0 diameter *in vivo*, imaging experiments were initiated by randomizing the animals into three groups.

***In Vivo* Optical Imaging.** The animals were randomized into groups I ($n = 7$), II ($n = 8$), and III ($n = 8$) with each group of animals designated for intravenous injection of 10 pmol QD equivalent/mouse of (a) unconjugated QD, (b) EGF-QD, and (c) GdCl$_3$ (10 mg/kg) 24 h prior to EGF-QD, respectively. *In vivo* optical imaging was performed using the IVIS imaging system 200 series (Xenogen Corporation, Hopkinton, MA) equipped with a 150 W quartz halogen excitation lamp, a cryogenically cooled (−105 °C), back-thinned, back-illuminated grade 1 CCD camera (26 × 26 mm) capable of imaging 2048 × 2048 pixels, heated stage, gas anesthesia ports. For the *in vivo* optical imaging of the fluorescence from QD nanoparticles and EGF-QD nanoprobes, the excitation and emission filters were set at 640 ± 25 and 840 ± 30 nm, respectively. The signal from the CCD is coupled to high-performance data acquisition software (Xenogen's Living Image). The collected fluorescence emission signal was stored in radiance units that refer to photons per second per centimeter squared per steridian (ph/s/cm^2/sr). The acquired fluorescence images were pseudocolored.

During the image acquisition process, the animals were kept anesthetized with 2% isoflurane, and the heated stage was maintained at 37 °C. After the background measurements were made, with the animals still anesthetized, 10 pmol QD equivalent/mouse of unconjugated QD (group I), EGF-QD (group II), and GdCl$_3$ (10 mg/kg) 24 h prior to EGF-QD (group III) was injected through the tail vein), and the animals were again imaged at 3, 15, and 30 min and 1, 1.5, 2, 3, 4, 6, 18, and 24 h postinjection. No signs of discomfort were observed during the injection or the entire experiment.

To extract QD fluorescence from the overlapping autofluorescence and background, the images were processed using ImageJ image-processing software from the U.S. National Institutes of Health (http://rsb.info.nih.gov/ij/) with the spectral unmixing algorithm plug-in. Two identically sized circular region of interests (ROIs) were selected: one overlying the tumor served as the target signal, and the other, in the corresponding shoulder, served as the background signal. The tumor-to-background ratio was calculated for each image at each time for all of the groups.

Euthanasia and Tissue Collection. Animals ($n = 4$) in each group were euthanized at 4 h postinjection by overdosing them with CO$_2$. Immediately after euthanasia, the organs were harvested, rinsed with PBS, and imaged using the IVIS imaging system. After image acquisition, the tissues were cut into two pieces. One piece of tissue was transferred to a vial containing 1 mL of PBS

and frozen until tissue homogenization. The other piece was embedded in a plastic cassette containing optimal cutting temperature medium and slowly cooled over dry ice and methanol. These embedded tissues were stored at −80 °C until they were sectioned into 5−7 μm thick slices on microscope slides for observation under the confocal microscope and for immunohistochemical analysis.

Tissue Homogenate. The frozen liver and tumor tissues from each group were thawed, and the PBS was discarded before measuring the wet weight. The weighed tissues were homogenized with 1 mL of freshly prepared 10 N NaOH to completely digest the cellular components. Of the resulting tissue homogenate, 300 μL was transferred to a flat-bottomed 96-well plate and imaged with the IVIS imaging system. The average radiance over the selected ROI was then measured using Living Image software. The QD signal in each organ was estimated on the basis of the weight of each organ.

Immunofluorescence. Immunofluorescence staining was performed to identify the effect of GdCl$_3$ on CD68, a marker for activated macrophages in the liver tissues. Frozen tissue slices were fixed in ice-cold acetone and blocked with protein blocking solution (100−400 μL) for 30 min at rt. Slides were incubated (1: 500 dilution) with rat monoclonal [FA-11] anti-CD68 antibody (Abcam Inc., Cambridge, MA) and washed with PBS (5 min × 3) and incubated with (1:200 dilution) fluorescein isothiocyanate (FITC)-conjugated Affinipure goat anti-rat immunoglobulin G (IgG) (Jackson ImmunoResearch, West Grove, PA) for 30 min at rt. After labeling with secondary antibody, the sections were washed with PBS (5 min × 3), dried, and covered with a coverslip using an antifade fluorescence mounting medium for confocal microscopy.

Confocal Microscopy. Laser-scanning confocal microscopy was performed using a Fluoview FV1000 confocal microscope (Olympus America Inc., Melville, NY) with a 60×/1.4 NA oil immersion objective (confocal aperture, 75 μm; aspect ratio, 1:1; image acquisition size, 512 × 512 pixels; image acquisition speed, 10 μs/pixel). Laser lines from a diode laser (FV5-LD405; Olympus America) at 405 nm and from an argon laser (FV10-COMB; Olympus America) at wavelengths of 458, 488, and 515 nm were used for excitation. The excitation laser beams were passed through a dichroic mirror (DM405/488/543), and the fluorescence emission was collected using a photomultiplier tube (PMT-R7862; Hamamatsu, Shizuoka, Japan) through a 650 nm barrier filter. Differential interference contrast images were acquired using a second photomultiplier tube (PMT- R7400; Hamamatsu, Shizuoka, Japan) with the same excitation laser beams. Both photomultiplier tubes were operated at a minimum gain level of 1 (to minimize the electronic noise), with operating voltage levels set at 610 and 115 V, respectively. The laser unit, confocal microscope, and detection units were connected to the computer and controlled using Fluoview software version 1.4 (FV10-ASW1.4, Olympus America), which was also used to perform the postacquisition data processing.

Statistical Analysis. Statistical analysis was performed using paired and unpaired t tests for comparisons between and within groups, respectively. Statistical significance was established at $P < 0.05$. Data are presented as the means ± SE.

Supporting Information Available: In vivo fluorescence images at 24 h postinjection of QD, EGF-QD, GdCl$_3$ pretreatment followed by EGF-QD and immunohistochemical quantification of CD68-positive Kupffer cells are shown in the Supporting Information. This material is available free of charge *via* the Internet at http://pubs.acs.org.

REFERENCES AND NOTES

1. Fass, L. Imaging and Cancer: A Review. *Mol. Oncol.* **2008**, *2*, 115–152.
2. Debbage, P.; Jaschke, W. Molecular Imaging with Nanoparticles: Giant Roles for Dwarf Actors. *Histochem. Cell Biol.* **2008**, *130*, 845–875.
3. Zhang, H.; Yee, D.; Wang, C. Quantum Dots for Cancer Diagnosis and Therapy: Biological and Clinical Perspectives. *Nanomedicine* **2008**, *3*, 83–91.
4. Bruchez, M., Jr.; Moronne, M.; Gin, P.; Weiss, S.; Alivisatos, A. P. Semiconductor Nanocrystals as Fluorescent Biological Labels. *Science* **1998**, *281*, 2013–2016.
5. Alivisatos, P. The Use of Nanocrystals in Biological Detection. *Nat. Biotechnol.* **2004**, *22*, 47–52.
6. Ballou, B.; Lagerholm, B. C.; Ernst, L. A.; Bruchez, M. P.; Waggoner, A. S. Noninvasive Imaging of Quantum Dots in Mice. *Bioconjugate Chem.* **2004**, *15*, 79–86.
7. Michalet, X.; Pinaud, F. F.; Bentolila, L. A.; Tsay, J. M.; Doose, S.; Li, J. J.; Sundaresan, G.; Wu, A. M.; Gambhir, S. S.; Weiss, S. Quantum Dots for Live Cells, *In Vivo* Imaging, and Diagnostics. *Science* **2005**, *307*, 538–544.
8. Akerman, M. E.; Chan, W. C.; Laakkonen, P.; Bhatia, S. N.; Ruoslahti, E. Nanocrystal Targeting *In Vivo*. *Proc. Natl. Acad. Sci. U.S.A.* **2002**, *99*, 12617–12621.
9. Papagiannaros, A.; Levchenko, T.; Hartner, W.; Mongayt, D.; Torchilin, V. Quantum Dots Encapsulated in Phospholipid Micelles for Imaging and Quantification of Tumors in the Near-Infrared Region. *Nanomedicine* **2009**, *5*, 216–224.
10. Mulder, W. J.; Castermans, K.; van Beijnum, J. R.; Oude Egbrink, M. G.; Chin, P. T.; Fayad, Z. A.; Lowik, C. W.; Kaijzel, E. L.; Que, I.; Storm, G.; Strijkers, G. J.; Griffioen, A. W.; Nicolay, K. Molecular Imaging of Tumor Angiogenesis Using Alphavbeta3-Integrin Targeted Multimodal Quantum Dots. *Angiogenesis* **2009**, *12*, 17–24.
11. Chen, K.; Li, Z. B.; Wang, H.; Cai, W.; Chen, X. Dual-Modality Optical and Positron Emission Tomography Imaging of Vascular Endothelial Growth Factor Receptor on Tumor Vasculature Using Quantum Dots. *Eur. J. Nucl. Med. Mol. Imaging* **2008**, *35*, 2235–2244.
12. Smith, B. R.; Cheng, Z.; De, A.; Koh, A. L.; Sinclair, R.; Gambhir, S. S. Real-Time Intravital Imaging of Rgd-Quantum Dot Binding to Luminal Endothelium in Mouse Tumor Neovasculature. *Nano Lett.* **2008**, *8*, 2599–2606.
13. Cai, W.; Shin, D. W.; Chen, K.; Gheysens, O.; Cao, Q.; Wang, S. X.; Gambhir, S. S.; Chen, X. Peptide-Labeled Near-Infrared Quantum Dots for Imaging Tumor Vasculature in Living Subjects. *Nano Lett.* **2006**, *6*, 669–676.
14. Morgan, N. Y.; English, S.; Chen, W.; Chernomordik, V.; Russo, A.; Smith, P. D.; Gandjbakhche, A. Real Time *In Vivo* Non-invasive Optical Imaging Using near-Infrared Fluorescent Quantum Dots. *Acad. Radiol.* **2005**, *12*, 313–323.
15. Robe, A.; Pic, E.; Lassalle, H. P.; Bezdetnaya, L.; Guillemin, F.; Marchal, F. Quantum Dots in Axillary Lymph Node Mapping: Biodistribution Study in Healthy Mice. *BMC Cancer* **2008**, *8*, 111.
16. Takeda, M.; Tada, H.; Higuchi, H.; Kobayashi, Y.; Kobayashi, M.; Sakurai, Y.; Ishida, T.; Ohuchi, N. *In Vivo* Single Molecular Imaging and Sentinel Node Navigation by Nanotechnology for Molecular Targeting Drug-Delivery Systems and Tailor-Made Medicine. *Breast Cancer* **2008**, *15*, 145–152.
17. Kim, S.; Lim, Y. T.; Soltesz, E. G.; De Grand, A. M.; Lee, J.; Nakayama, A.; Parker, J. A.; Mihaljevic, T.; Laurence, R. G.; Dor, D. M.; Cohn, L. H.; Bawendi, M. G.; Frangioni, J. V. Near-Infrared Fluorescent Type II Quantum Dots for Sentinel Lymph Node Mapping. *Nat. Biotechnol.* **2004**, *22*, 93–97.
18. Soltesz, E. G.; Kim, S.; Laurence, R. G.; DeGrand, A. M.; Parungo, C. P.; Dor, D. M.; Cohn, L. H.; Bawendi, M. G.; Frangioni, J. V.; Mihaljevic, T. Intraoperative Sentinel Lymph Node Mapping of the Lung Using Near-Infrared Fluorescent Quantum Dots. *Ann. Thorac. Surg.* **2005**, *79*, 269–277, discussion 269−277.

19. Soltesz, E. G.; Kim, S.; Kim, S. W.; Laurence, R. G.; De Grand, A. M.; Parungo, C. P.; Cohn, L. H.; Bawendi, M. G.; Frangioni, J. V. Sentinel Lymph Node Mapping of the Gastrointestinal Tract by Using Invisible Light. *Ann. Surg. Oncol.* **2006**, *13*, 386–396.

20. Parungo, C. P.; Ohnishi, S.; Kim, S. W.; Kim, S.; Laurence, R. G.; Soltesz, E. G.; Chen, F. Y.; Colson, Y. L.; Cohn, L. H.; Bawendi, M. G.; Frangioni, J. V. Intraoperative Identification of Esophageal Sentinel Lymph Nodes with Near-Infrared Fluorescence Imaging. *J. Thorac. Cardiovasc. Surg.* **2005**, *129*, 844–850.

21. Ballou, B.; Ernst, L. A.; Andreko, S.; Harper, T.; Fitzpatrick, J. A.; Waggoner, A. S.; Bruchez, M. P. Sentinel Lymph Node Imaging Using Quantum Dots in Mouse Tumor Models. *Bioconjugate Chem.* **2007**, *18*, 389–396.

22. Diagaradjane, P.; Orenstein-Cardona, J. M.; Colon-Casasnovas, N. E.; Deorukhkar, A.; Shentu, S.; Kuno, N.; Schwartz, D. L.; Gelovani, J. G.; Krishnan, S. Imaging Epidermal Growth Factor Receptor Expression *In Vivo*: Pharmacokinetic and Biodistribution Characterization of a Bioconjugated Quantum Dot Nanoprobe. *Clin. Cancer Res.* **2008**, *14*, 731–741.

23. Gao, X.; Cui, Y.; Levenson, R. M.; Chung, L. W.; Nie, S. *In Vivo* Cancer Targeting and Imaging with Semiconductor Quantum Dots. *Nat. Biotechnol.* **2004**, *22*, 969–976.

24. Lidke, D. S.; Nagy, P.; Heintzmann, R.; Arndt-Jovin, D. J.; Post, J. N.; Grecco, H. E.; Jares-Erijman, E. A.; Jovin, T. M. Quantum Dot Ligands Provide New Insights into Erbb/Her Receptor-Mediated Signal Transduction. *Nat. Biotechnol.* **2004**, *22*, 198–203.

25. Barat, B.; Sirk, S. J.; McCabe, K. E.; Li, J.; Lepin, E. J.; Remenyi, R.; Koh, A. L.; Olafsen, T.; Gambhir, S. S.; Weiss, S.; Wu, A. M., Cys-Diabody Quantum Dot Conjugates (ImmunoQdots) for Cancer Marker Detection. *Bioconjugate Chem.* **2009**, *20*, 1474−1481.

26. Shi, C.; Zhu, Y.; Xie, Z.; Qian, W.; Hsieh, C. L.; Nie, S.; Su, Y.; Zhau, H. E.; Chung, L. W. Visualizing Human Prostate Cancer Cells in Mouse Skeleton Using Bioconjugated Near-Infrared Fluorescent Quantum Dots. *Urology* **2009**, *74*, 446–451.

27. Wang, J.; Yong, W. H.; Sun, Y.; Vernier, P. T.; Koeffler, H. P.; Gundersen, M. A.; Marcu, L. Receptor-Targeted Quantum Dots: Fluorescent Probes for Brain Tumor Diagnosis. *J. Biomed. Opt.* **2007**, *12*, 044021.

28. Wu, X.; Liu, H.; Liu, J.; Haley, K. N.; Treadway, J. A.; Larson, J. P.; Ge, N.; Peale, F.; Bruchez, M. P. Immunofluorescent Labeling of Cancer Marker Her2 and Other Cellular Targets with Semiconductor Quantum Dots. *Nat. Biotechnol.* **2003**, *21*, 41–46.

29. Sen, D.; Deerinck, T. J.; Ellisman, M. H.; Parker, I.; Cahalan, M. D. Quantum Dots for Tracking Dendritic Cells and Priming an Immune Response *In Vitro* and *In Vivo*. *PLoS One* **2008**, *3*, e3290.

30. Schipper, M. L.; Cheng, Z.; Lee, S. W.; Bentolila, L. A.; Iyer, G.; Rao, J.; Chen, X.; Wu, A. M.; Weiss, S.; Gambhir, S. S. Micropet-Based Biodistribution of Quantum Dots in Living Mice. *J. Nucl. Med.* **2007**, *48*, 1511–1518.

31. Lewinski, N.; Colvin, V.; Drezek, R. Cytotoxicity of Nanoparticles. *Small* **2008**, *4*, 26–49.

32. Hardman, R. A Toxicologic Review of Quantum Dots: Toxicity Depends on Physicochemical and Environmental Factors. *Environ. Health Perspect.* **2006**, *114*, 165–172.

33. Harris, J. M.; Chess, R. B. Effect of Pegylation on Pharmaceuticals. *Nat. Rev. Drug Discovery* **2003**, *2*, 214–221.

34. Greenwald, R. B. PEG Drugs: An Overview. *J. Controlled Release* **2001**, *74*, 159–171.

35. Brigger, I.; Dubernet, C.; Couvreur, P. Nanoparticles in Cancer Therapy and Diagnosis. *Adv. Drug Delivery Rev.* **2002**, *54*, 631–651.

36. Proffitt, R. T.; Williams, L. E.; Presant, C. A.; Tin, G. W.; Uliana, J. A.; Gamble, R. C.; Baldeschwieler, J. D. Liposomal Blockade of the Reticuloendothelial System: Improved Tumor Imaging with Small Unilamellar Vesicles. *Science* **1983**, *220*, 502–505.

37. Hamori, C. J.; Lasic, D. D.; Vreman, H. J.; Stevenson, D. K. Targeting Zinc Protoporphyrin Liposomes to the Spleen Using Reticuloendothelial Blockade with Blank Liposomes. *Pediatr. Res.* **1993**, *34*, 1–5.

38. Gregoriadis, G.; Neerunjun, D. E. Control of the Rate of Hepatic Uptake and Catabolism of Liposome-Entrapped Proteins Injected into Rats. Possible Therapeutic Applications. *Eur. J. Biochem.* **1974**, *47*, 179–185.

39. Souhami, R. L.; Patel, H. M.; Ryman, B. E. The Effect of Reticuloendothelial Blockade on the Blood Clearance and Tissue Distribution of Liposomes. *Biochim. Biophys. Acta* **1981**, *674*, 354–371.

40. Gregoriadis, G.; Neerunjun, D. E.; Hunt, R. Fate of a Liposome-Associated Agent Injected into Normal and Tumour-Bearing Rodents. Attempts To Improve Localization in Tumour Tissues. *Life Sci.* **1977**, *21*, 357–369.

41. Husztik, E.; Lazar, G.; Parducz, A. Electron Microscopic Study of Kupffer-Cell Phagocytosis Blockade Induced by Gadolinium Chloride. *Br. J. Exp. Pathol.* **1980**, *61*, 624–630.

42. Iimuro, Y.; Yamamoto, M.; Kohno, H.; Itakura, J.; Fujii, H.; Matsumoto, Y. Blockade of Liver Macrophages by Gadolinium Chloride Reduces Lethality in Endotoxemic Rats—Analysis of Mechanisms of Lethality in Endotoxemia. *J. Leukocyte Biol.* **1994**, *55*, 723–728.

43. Abraham, S.; Szabo, A.; Kaszaki, J.; Varga, R.; Eder, K.; Duda, E.; Lazar, G.; Tiszlavicz, L.; Boros, M.; Lazar, G., Jr. Kupffer Cell Blockade Improves the Endotoxin-Induced Microcirculatory Inflammatory Response in Obstructive Jaundice. *Shock* **2008**, *30*, 69–74.

44. Usynin, I. F.; Khar'kovsky, A. V.; Balitskaya, N. I.; Panin, L. E. Gadolinium Chloride-Induced Kupffer Cell Blockade Increases Uptake of Oxidized Low-Density Lipoproteins by Rat Heart and Aorta. *Biochemistry (Moscow)* **1999**, *64*, 620–624.

45. Ding, H.; Tong, J.; Wu, S. C.; Yin, D. K.; Yuan, X. F.; Wu, J. Y.; Chen, J.; Shi, G. G. Modulation of Kupffer Cells on Hepatic Drug Metabolism. *World J. Gastroenterol.* **2004**, *10*, 1325–1328.

46. Ruttinger, D.; Vollmar, B.; Wanner, G. A.; Messmer, K. *In Vivo* Assessment of Hepatic Alterations Following Gadolinium Chloride-Induced Kupffer Cell Blockade. *J. Hepatol.* **1996**, *25*, 960–967.

47. Lazar, G., Jr.; Lazar, G.; Kaszaki, J.; Olah, J.; Kiss, I.; Husztik, E. Inhibition of Anaphylactic Shock by Gadolinium Chloride-Induced Kupffer Cell Blockade. *Agents Actions* **1994**, *41*, C97–C98.

48. Giakoustidis, D. E.; Iliadis, S.; Tsantilas, D.; Papageorgiou, G.; Kontos, N.; Kostopoulou, E.; Botsoglou, N. A.; Gerasimidis, T.; Dimitriadou, A. Blockade of Kupffer Cells by Gadolinium Chloride Reduces Lipid Peroxidation and Protects Liver from Ischemia/Reperfusion Injury. *Hepatogastroenterology* **2003**, *50*, 1587–1592.

49. Spencer, A.; Wilson, S.; Harpur, E. Gadolinium Chloride Toxicity in the Mouse. *Hum. Exp. Toxicol.* **1998**, *17*, 633–637.

50. Maeda, H.; Fang, J.; Inutsuka, T.; Kitamoto, Y. Vascular Permeability Enhancement in Solid Tumor: Various Factors, Mechanisms Involved and Its Implications. *Int. Immunopharmacol.* **2003**, *3*, 319–328.

51. Smith, A. M.; Duan, H.; Mohs, A. M.; Nie, S. Bioconjugated Quantum Dots for *In Vivo* Molecular and Cellular Imaging. *Adv. Drug Delivery Rev.* **2008**, *60*, 1226–1240.

52. Faure, A. C.; Dufort, S.; Josserand, V.; Perriat, P.; Coll, J. L.; Roux, S.; Tillement, O. Control of the *In Vivo* Biodistribution of Hybrid Nanoparticles with Different Poly(ethylene glycol) Coatings. *Small* **2009**, *5*, 2565–2575.

53. van Schooneveld, M. M.; Vucic, E.; Koole, R.; Zhou, Y.; Stocks, J.; Cormode, D. P.; Tang, C. Y.; Gordon, R. E.; Nicolay, K.; Meijerink, A.; Fayad, Z. A.; Mulder, W. J. Improved Biocompatibility and Pharmacokinetics of Silica Nanoparticles by Means of a Lipid Coating: A Multimodality Investigation. *Nano Lett.* **2008**, *8*, 2517–2525.

54. Li, S. D.; Huang, L. Pharmacokinetics and Biodistribution of Nanoparticles. *Mol. Pharmaceutics* **2008**, *5*, 496–504.

55. Bailey, R. E.; Smith, A. M.; Nie, S. M. Quantum Dots in Biology and Medicine. *Physica E* **2004**, *25*, 1–12.

56. Clift, M. J.; Rothen-Rutishauser, B.; Brown, D. M.; Duffin, R.; Donaldson, K.; Proudfoot, L.; Guy, K.; Stone, V. The Impact of Different Nanoparticle Surface Chemistry and Size on Uptake and Toxicity in a Murine Macrophage Cell Line. *Toxicol. Appl. Pharmacol.* **2008**, *232*, 418–427.

57. Patel, K. R.; Li, M. P.; Baldeschwieler, J. D. Suppression of Liver Uptake of Liposomes by Dextran Sulfate 500. *Proc. Natl. Acad. Sci. U.S.A.* **1983**, *80*, 6518–6522.

58. Choi, H. S.; Liu, W.; Misra, P.; Tanaka, E.; Zimmer, J. P.; Itty Ipe, B.; Bawendi, M. G.; Frangioni, J. V. Renal Clearance of Quantum Dots. *Nat. Biotechnol.* **2007**, *25*, 1165–1170.

59. Lim, Y. T.; Kim, S.; Nakayama, A.; Stott, N. E.; Bawendi, M. G.; Frangioni, J. V. Selection of Quantum Dot Wavelengths for Biomedical Assays and Imaging. *Mol. Imaging* **2003**, *2*, 50–64.

60. Krohn, N.; Kapoor, S.; Enami, Y.; Follenzi, A.; Bandi, S.; Joseph, B.; Gupta, S. Hepatocyte Transplantation-Induced Liver Inflammation Is Driven by Cytokines-Chemokines Associated with Neutrophils and Kupffer Cells. *Gastroenterology* **2009**, *136*, 1806–1817.

61. Chung, K. Y.; Jeong, G. Y.; Choi, K. B.; Sung, S. H.; Kim, Y. S. Prevention of Primary Nonfunction after Canine Liver Allotransplantation: The Effect of Gadolinium Chloride. *Transplant Proc.* **2004**, *36*, 1928–1930.

62. von Frankenberg, M.; Golling, M.; Mehrabi, A.; Nentwich, H.; Klar, E.; Kraus, T. W. Donor Pretreatment with Gadolinium Chloride Improves Early Graft Function and Survival after Porcine Liver Transplantation. *Transplant Int.* **2003**, *16*, 806–813.